CHAPTER – 5

STRUCTURAL TRANSITION AND SOFTENING IN Al-Fe INTERMETALLIC COMPOUNDS

Chapter – 5

STRUCTURAL TRANSITION AND SOFTENING IN Al-Fe INTERMETALLIC COMPOUNDS*

In the phase diagram of an Al-Fe, there are many iron aluminide intermetallic compounds, such as $AlFe_3$, AlFe, Al_2Fe, Al_5Fe_2 and $Al_{13}Fe_4$ (or Al_3Fe) [Massalski (1994)]. The currently accepted Al-Fe phase diagram appears in Fig. 5.1 [Kattner *et al.* (1990)].

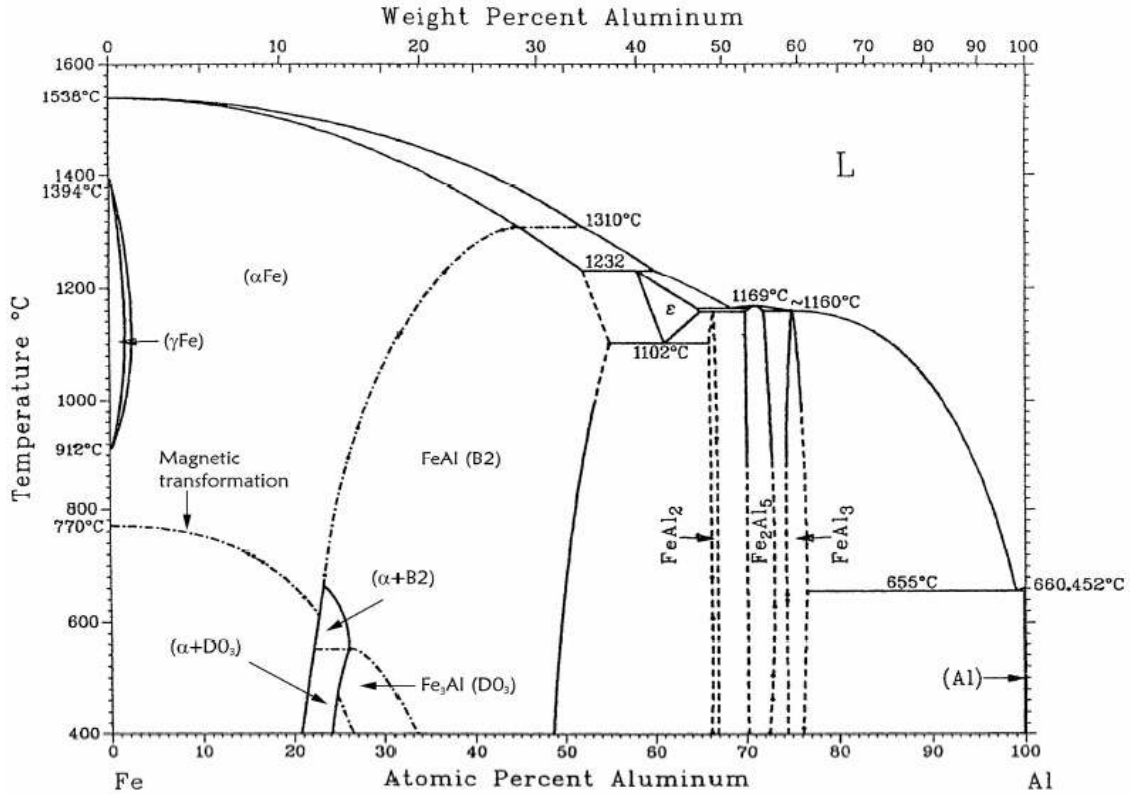

Figure 5.1: Phase diagram of the Al-Fe system [Kattner *et al.* (1990)].

*A part of this work is published in *Materials Science and Engineering A* **638**, 282-288 (2015).

The objective of the present investigation is to develop a better understanding of the mechanisms of evolution of phases and ensuing properties during amorphization process in iron alumindies, particularly corresponding to Al_3Fe and Al_2Fe intermetallic phases driven far from equilibrium e.g. by high energy mechanical milling. The crystalline-to-amorphous transformations were monitored through different stages of milling of the as-cast intermetallics. The structural aspects and the mechanical properties were evaluated by microhardness and nanoindentation by collecting materials at different milling intervals.

5.1 Structural evolution during milling

The X-ray diffraction pattern of crushed as-cast powders of Al–25 at.%Fe alloy is shown in Fig. 5.2. Diffraction peaks confirm mostly single phase complex monoclinic Al_3Fe (θ) intermetallic. The JCPDS (Joint Committee on Powder Diffraction Standards) data suggests that this compound is Al_3Fe with a monoclinic structure. According to the original structural model of Al_3Fe by Grin *et al*. (1994), lattice parameters of the monoclinic unit cell (space group C2m, Pearson symbol mC102) are a=1.5492 nm, b=0.8078 nm, c=1.2471nm, and $\beta=107.69^o$ with 102 atoms in the unit cell distributed over 5 Fe and 15 Al crystallographic sites. The structural evolution of Al_3Fe intermetallic subjected to varying hours of MM is shown in Fig. 5.3. At early stages of milling, the peaks are relatively broad because of the fine crystallite size and the presence of strain in the powder. After 10 to 20 h of milling, formation of η-Al_5Fe_2 was observed as an intermediate phase. The presence of η-Al_5Fe_2 prevailed till 30 h of milling but further increase in milling time led to the broadening of these peaks too. The intermetallic Al_3Fe phase was completely transformed into the

amorphous state after 50 h of milling. As can be seen from the XRD patterns in Fig. 5.3, a broad halo at $2\theta = 40\text{-}47^{o}$ suggests formation of an amorphous phase. Eventually, the phase transformations during MM for Al–25 at.%Fe alloy powders can be schematically expressed as shown in Fig.5.4.

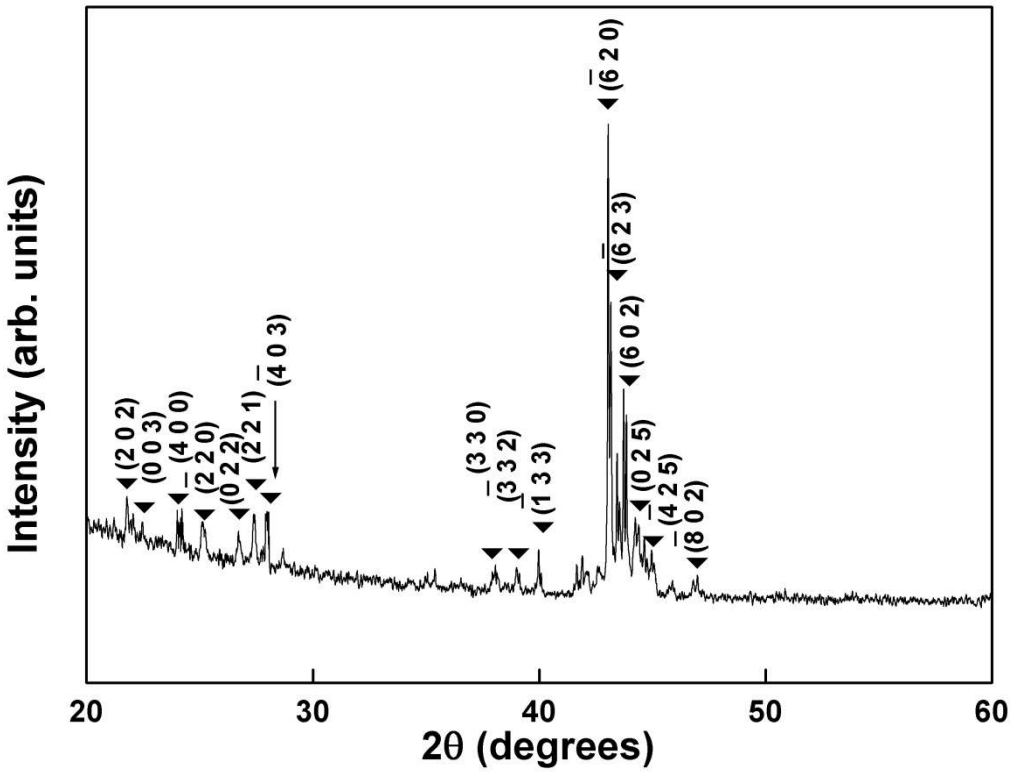

Figure 5.2: XRD pattern of Al-25 at.%Fe as-cast alloy showing single θ-Al_3Fe intermetallic phase.

Miedema model [Niessen *et al*. (1983)] predicts that an amorphous phase can form in the composition range of 25 to 60 at.% Fe in the Al-Fe system, which is in agreement with the present work. For Al–25 at.%Fe alloy, the results indicate that the monoclinic Al_3Fe intermetallic phase which is stable at ambient temperature becomes unstable with MM and get transformed to orthorhombic Al_5Fe_2 phase. The phase

transformation observed can be attributed to the accumulation of structural defects which increase the energy stored in the intermetallic phase, as a result increases the lattice entropy favoring the formation of Al_5Fe_2. Further, the enthalpies of formation for

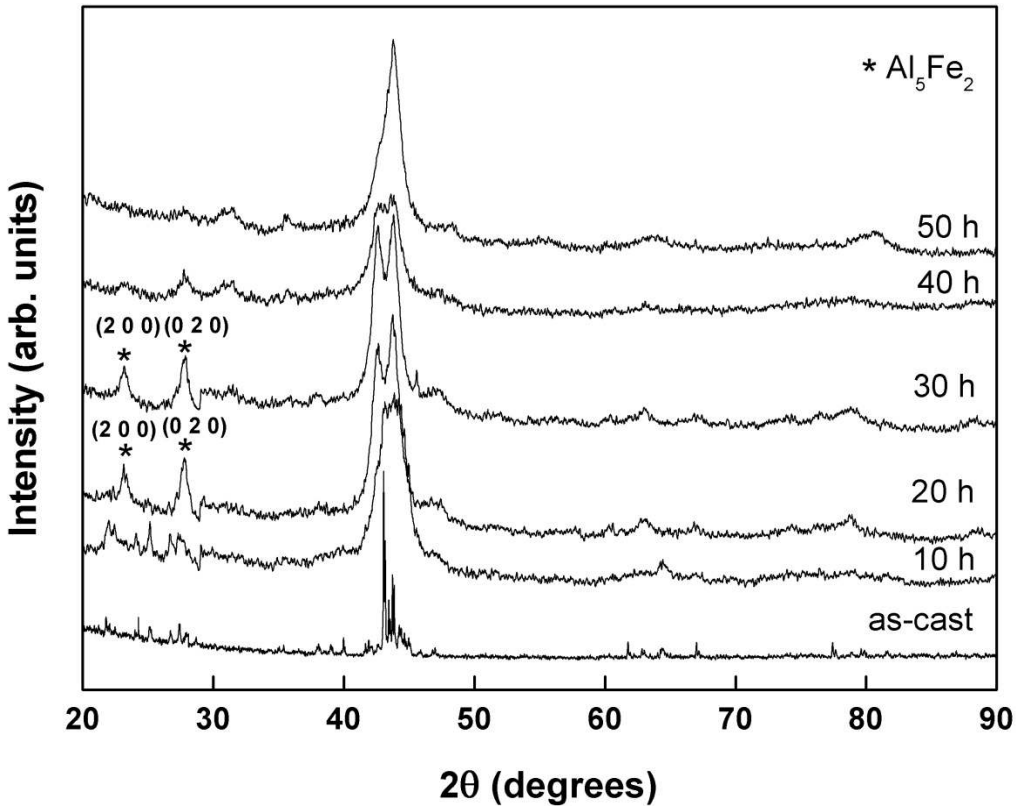

Figure 5.3: XRD patterns showing structural evolution of θ-Al_3Fe intermetallic phase during MM.

orthorhombic Al_5Fe_2 phase (ΔH_f = -28.3 kJ/mol) and monoclinic Al_3Fe phase (ΔH_f = -28.1 kJ/mol) are very close and found slightly less endothermic for Al_5Fe_2 than Al_3Fe analogue, which show that Al_5Fe_2 phase are energetically stable relative to the Al_3Fe phase [De Boer *et al*. (1989)].

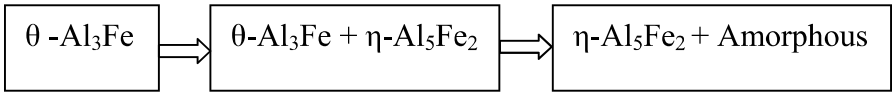

Figure 5.4: Structural evolution of Al–25 at.%Fe alloy powders during MM.

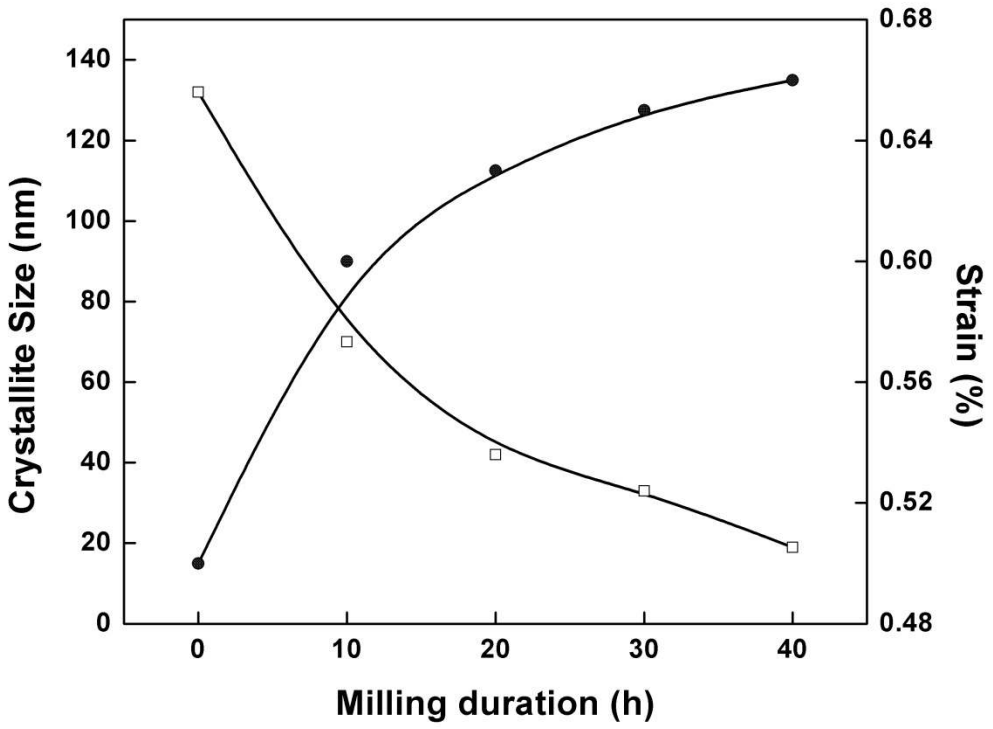

Figure 5.5: Variation of crystallite size and strain with milling duration for Al–25 at.%Fe showing a decrease in crystallite size and an increase in strain with milling duration.

The average crystallite size of the as-milled powders calculated for each condition from the X-ray diffraction patterns, decreased with milling duration along

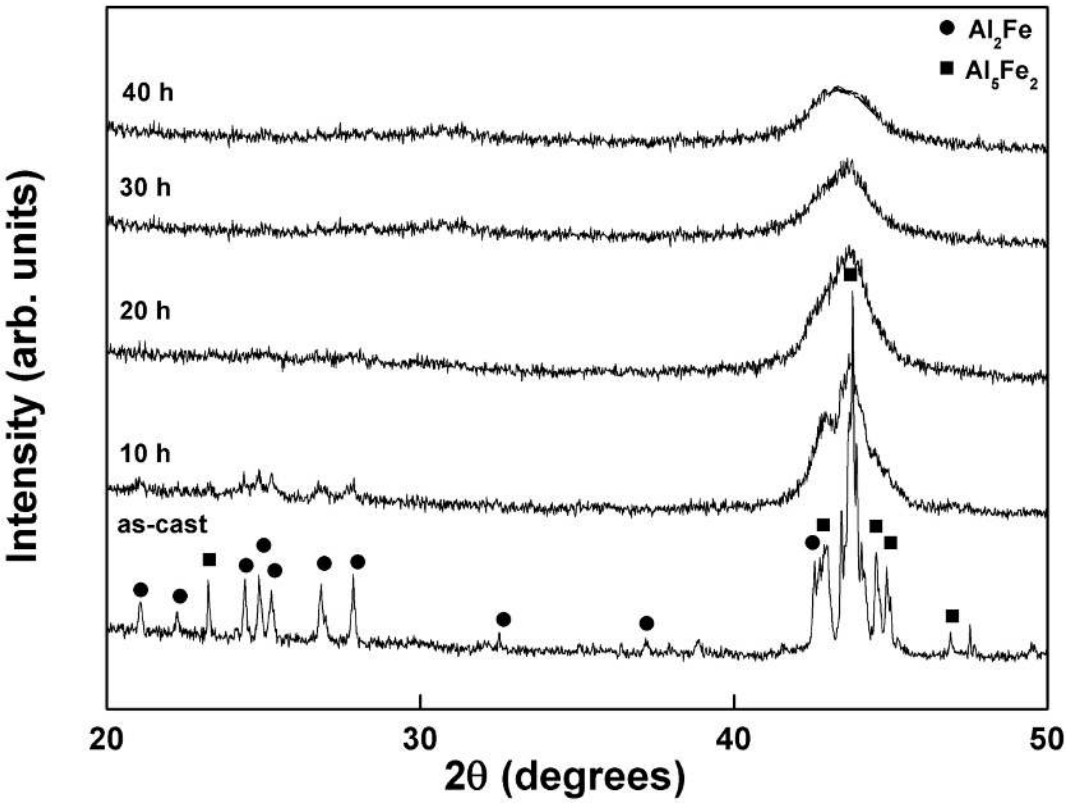

Figure 5.6: XRD patterns Al-35.4 at.%Fe as-cast alloy and after mechanically milled for 10, 20, 30 and 40 h showing structural evolution with milling time.

with a corresponding increase in lattice strain as shown in Fig. 5.5 for the Al–25 at.%Fe alloy. The results suggest the presence of crystals of about 19 nm size after milling for Al-34.5 at.%Fe alloy is shown in Fig. 5.6. Diffraction peak confirms mixture of intermetallic phases namely ζ-Al_2Fe and η-Al_5Fe_2. JCPDS data suggests that the compound is representative of Al_2Fe triclinic phase (JCPDS 00-033-0019) with lattice parameters of a = 0.7609 nm, b = 1.691 nm, c = 0.4869 nm and Al_5Fe_2 orthorhombic phase (JCPDS 00-047-1435) with cell parameters of a = 0.7648 nm, b = 0.6413 nm and c = 0.4216 nm. The compound Al_2Fe has the lowest possible symmetry crystal

structure, triclinic (Pearson symbol aP19) [Corby *et al*. (1973)] and therefore transforms to a high symmetry phase Al_5Fe_2 orthorhombic (Pearson symbol oC24) in the nearby composition. Stability calculations utilizing first principles total energy predict that the aP19 structure loses stability to the oC24 structure at elevated temperatures and this occurs because oC24 structure has a much lower atomic density than aP19 structure resulting in high vibrational entropy [Mihalkovic *et al*. (2012)]. Intermetallic phase Al_5Fe_2 along with Al_2Fe was also observed by Gasior *et al*. (2012) for a composition range of 34.7 to 35.3 at.%Fe in Al alloy. In Al-34.5 at.%Fe alloy, 10 h of MM leads to a phase transformation from crystalline triclinic Al_2Fe and orthorhombic Al_5Fe_2 to partial formation of amorphous phase. The width observed in the most intense diffraction peak, can also be attributed to the peak overlapping from the mixture of intermetallic phases. On further milling, the width of Bragg peaks decreases and peaks resolution increase to resolve the most intense reflections of Al_5Fe_2 intermetalic indicating that Al_2Fe intermetallic phase becomes unstable as a result of MM. As mentioned earlier, the accumulation of structural defects which increase the energy stored in the intermetallic material during the milling process lead to the detected phase transition. However, amorphization was observed with prolonged milling time and after 40 h of milling complete amorphization was achieved in this

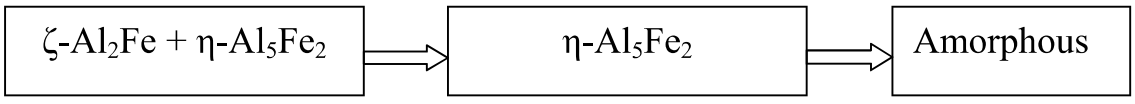

Figure 5.7: Structural evolution of Al-34.5 at.%Fe alloy powders during MM.

particular composition, as is evident in Fig. 5.6. It is worthy to note that the powders of this particular composition became pyrophoric in nature after 40 h of milling, and this can be ascribed to the very fine size and consequently large surface area induced by MM. This was observed even as the milling experiments were periodically stopped at regular intervals of every 30 minutes. The phase transformation achieved by milling Al-34.5 at.%Fe alloy powders can be schematically represented as shown in Fig. 5.7.

The milling process thus clearly demonstrates that under the present milling conditions Al_5Fe_2 phase is stable with respect to competing phases and its orthorhombic structure featuring a rigid framework of fully occupied Al and Fe sites as well as partially occupied Al sites confine within channels [Gu *et al*. (2006)] that thread through the structure makes this phase also unstable when subjected to severe plastic deformation leading to amorphous phase. It is proposed that intermetallic compounds with narrow homogeneity ranges tend to become amorphous [Schwarz *et al*. (1986)] due to lattice defects introduced by MM which promote spontaneous transformation to the amorphous phase.

5.2 Microstructural evolution

The external morphology of milled intermetallic powders was examined using SEM. The samples were prepared by sprinkling the loose powder on an adhesive stub and then examined using secondary electron imaging mode. Fig. 5.8(a) and (b) shows SEM micrographs of Al-25 at.%Fe powder particles milled for 50 h and Al-34.5 at.%Fe powders milled for 40 h. The micrographs show agglomerates composed of fine particles suggesting that a transition from coarse-to-fine grained structure has occurred. Comparison between the evolution of microstructure and morphologies in Fig. 5.8(a)

and (b) shows that the refinement of the microstructure in Al-34.5 at.%Fe was faster at lower milling time (40 h) than at 50 h of milling for Al-25 at.%Fe. Fig. 5.9(a) shows the TEM image of Al-25 at.%Fe alloy milled for 50 h. The microstructure shows co-

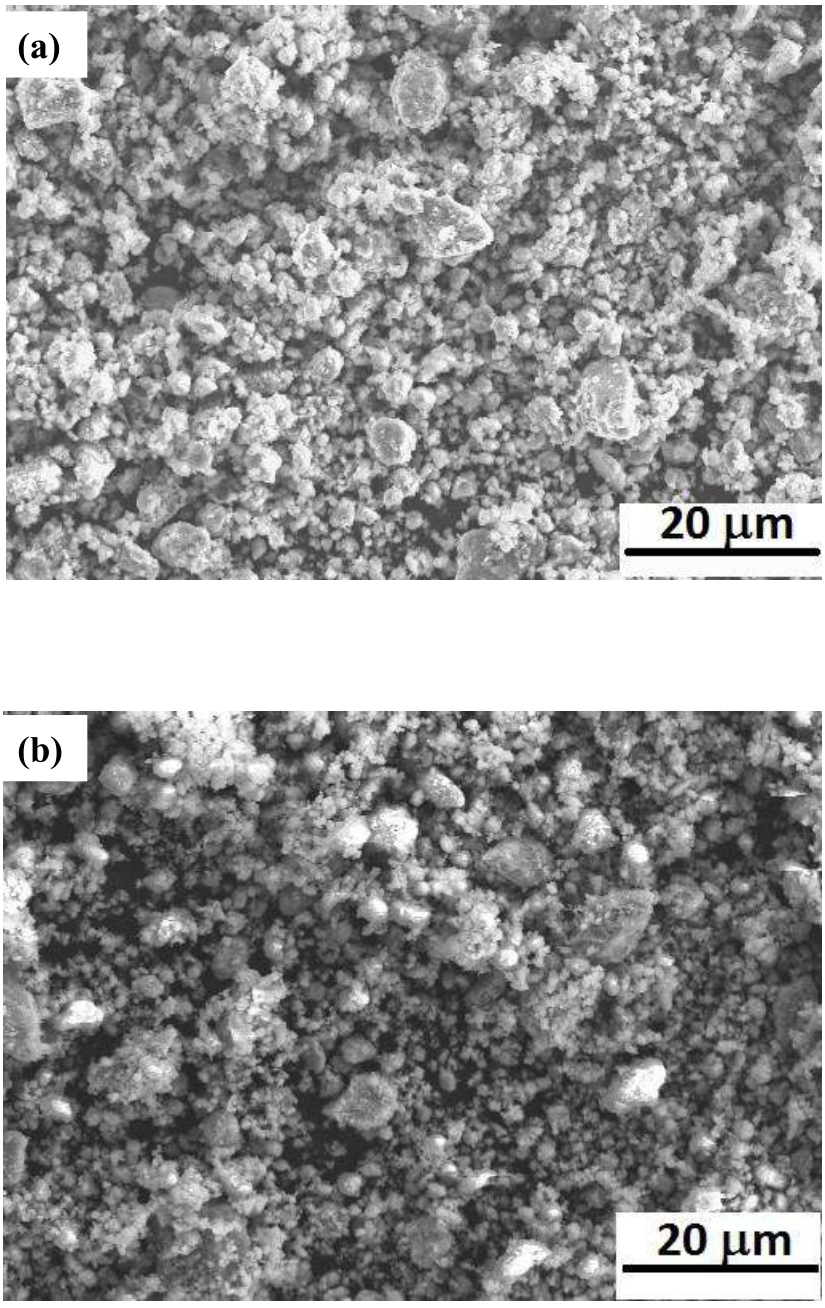

Figure 5.8: SEM micrographs of final milled powders of (a) Al-25 at.%Fe and (b) Al-34.5 at.%Fe alloy.

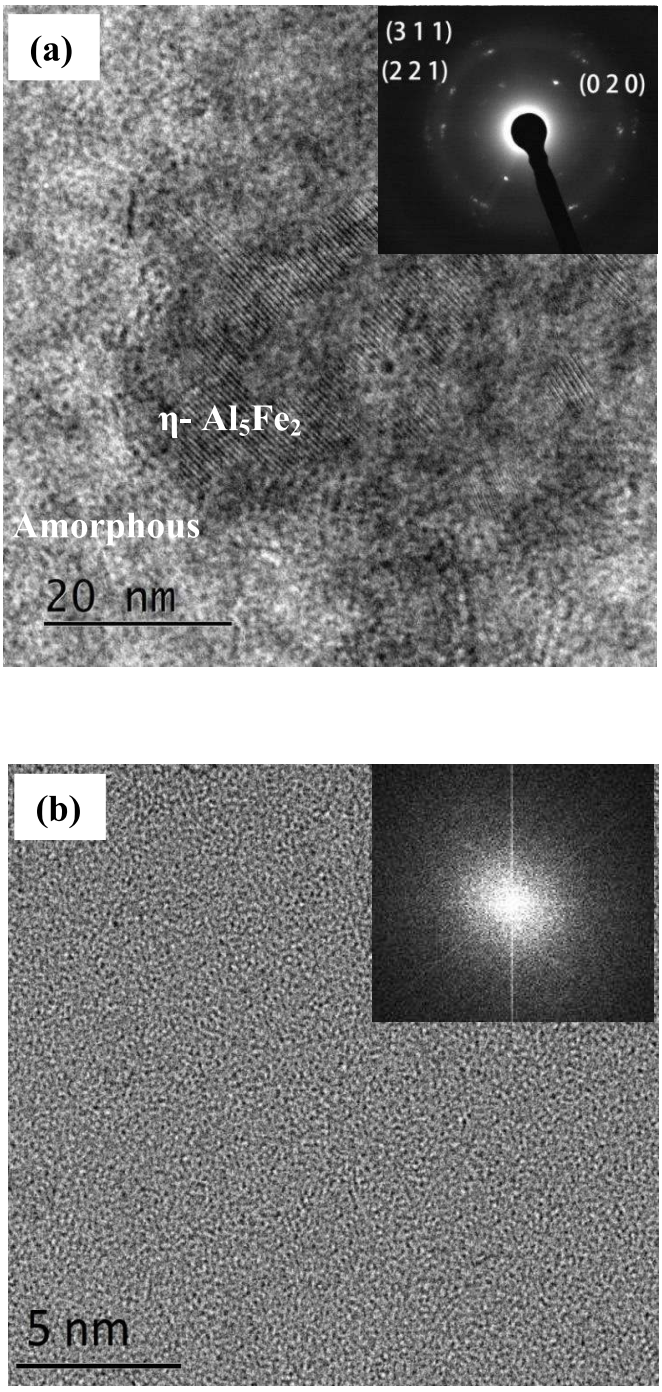

Figure 5.9: (a) TEM image of 50 h milled product of Al-25 at.%Fe alloy showing crystalline η- Al_5Fe_2 and amorphous phase and its corresponding SAD pattern and (b) a HRTEM image and the corresponding FFT-SAD of Al-35.4 at.%Fe showing a complete amorphous phase after 40 h of milling.

existence of both amorphous and nanocrystalline, η-Al_5Fe_2 phases and the SAD pattern indicates diffuse ring along with diffraction spots. However, in its corresponding XRD pattern it indicated complete amorphization after 50 h of milling. It can be stated that broadening of the peak observed in XRD not only corresponds to formation of amorphous structure but also to the refinement of the nanocrystalline structure induced by high energy ball milling and so residual crystalline phase is present along with amorphous phase. Fig. 5.9(b) shows a high resolution TEM micrograph corresponding to Al-34.5 at.%Fe alloy milled for 40 h. The micrograph reveals single amorphous phase and is corroborated by the Fast Fourier transformation-selected area diffraction (FFT-SAD) pattern.

5.3 Thermodynamic analysis

The possibility of formation of amorphous phase by calculating the Gibbs free energies of formation of the metastable amorphous phase, intermetallic and crystalline solid solution has been explored, using extended Miedema's model [Niessen *et al.* (1983) and Miedema *et al.* (1980)] and improved model proposed by Zhang *et. al.* (2002) to predict the phase equilibrium considering both chemical and interfacial contributions for Al-Fe alloys subjected to mechanical milling. The model-based predictions and experimental results have been utilized to understand the phase formation by mechanical milling of the powder blend.

5.3.1 Extended Miedema's model

Thermodynamic calculations for determining the Gibbs free energy for solid solution, intermetallic and that of the amorphous phase was carried out to indicate the glass forming range. ΔH_S, enthalpy of solid solution phase is calculated from modified Miedema model [Niessen *et al.* (1988), Lin *et al.* (2000) and Varin *et al.* (2003)]. For crystalline state the Gibbs energy (ΔG_{crys}) can be expressed in terms of solid solution (ΔG_S) and interfacial/grain boundary energies (ΔG_γ) as:

$$\Delta G_{crys} = \Delta G_S + \Delta G_\gamma \quad (5.1)$$

ΔH_S and ΔS_S are the enthalpy and entropy of mixing, respectively, whereas ΔG_γ terms refer to interfacial contributions, such that $\Delta G_\gamma = 4\,\gamma\,\frac{V_m}{d_c}$, where d_c represents average grain size and γ is the interfacial energy [Schwarz *et al.* (1986) and Murr (1975)]. The entropy of mixing for an ideal solution is given by:

$$\Delta S_S = -R(X_A\, lnX_A + X_B\, lnX_B) \quad (5.2)$$

Where X_A and X_B are the molar fraction of elements A and B, and R is the universal gas constant. The enthalpy of formation of a solid solution is given as [Niessen *et al.* (1988) and Miedema *et al.* (1981)]:

$$\Delta H_S^{AB} = \Delta H_c^{AB} + \Delta H_e^{AB} + \Delta H_{str.}^{AB} \quad (5.3)$$

Where ΔH_c, ΔH_e and $\Delta H_{str.}$ are the chemical, elastic and structural contributions due to mixing of the different atoms, the atom size mismatch and the difference in valency and crystal structure of solute and solvent respectively. Compared with the first two items, the structural contributions have only a minor effect [Lopez *et al.* (1987)], and therefore $\Delta H_{str.}^{AB}$ can be ignored.

$$\Delta H_S^{AB} = \Delta H_c^{AB} + \Delta H_e^{AB} \quad (5.4)$$

From the Miedema and Niessen model ΔH_c^{AB} is given by the equation [Niessen *et al.* (1988), Miedema *et al.* (1981)]:

$$\Delta H_c^{AB} = X_A X_B (f_B^A \Delta H_{sol}^{A\,in\,B} + f_A^B \Delta H_{sol}^{B\,in\,A}) \tag{5.5}$$

$\Delta H_{sol}^{A\,in\,B}$ is the solution enthalpy of A in B given by:

$$\Delta H_{sol}^{A\,in\,B} = \left[\frac{V_A^{2/3}}{(n_{ws}^{-1/3})_{av}}\right][-p(\Delta\phi)^2 + Q(n_{ws}^{1/3})^2] \tag{5.6}$$

Where f_B^A and C_B are given by the equations:

$$f_B^A = C_B[1 + k(C_A C_B)^2] \tag{5.7}$$

$$C_B = \frac{X_B V_B^{2/3}}{X_B V_B^{2/3} + X_A V_A^{2/3}} \tag{5.8}$$

Where V, Φ and n_{ws} represents the molar volume, work function and electron density of the constituents. f_B^A is the degree by which A atom is surrounded by B atoms and C is the surface concentration of atom. p and Q are the empirical constants having the same value for widely different metal combinations. The value of k is taken to be 5 for short-range order (amorphous) and 8 for long-range order, respectively.

$$\Delta H_e^{AB} = X_A X_B (f_B^A E_e^{A\,in\,B} + f_A^B E_e^{B\,in\,A}) \tag{5.9}$$

Where $E_e^{A\,in\,B}$ is the size mismatch contribution to the enthalpy of solution of A in B per mole A, which is given by the equation [Niessen *et al.* (1983)]:

$$\Delta E_e^{A\,in\,B} = \frac{\{2K_A\mu_B(V_B - V_A)^2\}}{\{3K_A V_A + 4\mu_B V_A\}} \tag{5.10}$$

Where K, μ, are bulk modulus, shear modulus, respectively. The Enthalpy of formation of the amorphous phase for binary system can be estimated from:

$$\Delta H_{amorphous} = \Delta H_{chem} + 3.5(X_A T_{m,A} + X_B T_{m,B}) \tag{5.11}$$

For binary systems Gibbs free energy of formation of the amorphous phase is given by the equation:

$$\Delta G_a = \Delta H_a - T\Delta S_a + X_A \Delta G_A^{a-c}(T) + X_B \Delta G_B^{a-c}(T) \quad (5.12)$$

ΔH_a and ΔS_a are the enthalpy and entropy of mixing of the amorphous phase. The term $\Delta G_i^{a-c}(T)$ is the difference in Gibbs free energy between the amorphous and crystalline phases of the pure element at the room temperature. ΔH_a contains only the chemical contribution due to the amorphous structure, which can be calculated from equation 5.5 using a value of 5 for the constant k. ΔS_a can be calculated from equation 5.2.

Because the MA/MM experiments are carried out at room temperature, so it can be assumed that the temperature of MA/MM was at room temperature. $\Delta G_{a\text{-}c}\ (T)$ can be estimated from equation:

$$\Delta G^{a-c}(T) = \frac{K_{corr}\Delta H_f(T_m - T)}{T_m} \quad (5.13)$$

Where ΔH_f and T_m are enthalpy of fusion and melting temperature respectively and K_{corr} is the correction coefficient, which can be represented by the equation [Singh *et al.* (1983)]:

$$K_{corr} = \frac{7T}{6T + T_m} \quad (5.14)$$

5.3.2 Improved Miedema's model (Zhang model)

In order to calculate the standard formation enthalpy of the intermetallic compounds, the heat of solution of one constituent metal in its partner metal of a binary transition-metal system is crucial, and consists of two important parameters, i.e., the electron-negativity difference and the solubility [Miedema *et al.* (1980) and Miedema *et al.* (1989)]. First, the electronegativity difference between the two constituent metals is a negative parameter, which provides a major driving force for the formation of an intermetallic compound. When two different metallic atoms are brought into contact,

the charge redistribution is not limited within the inside of each atom, but will include a net charge transfer, which is governed by the difference in contact potential between the two dissimilar metals. The charge will flow along a potential gradient from high to low, until the resultant dipole layer compensates the potential difference. Viewing at an atomic scale, the charge transfer corresponds to a negative ionic contribution to the heat of solution, which can be expressed by the electronegativity difference between the two constituent metals, $\Delta\phi^*$. Second, when transferring atoms of metal B into metal A for forming an A–B alloy, the discontinuity of the electron density at the boundaries between the dissimilar atoms, which is defined as $\Delta n_{WS}^{1/2}$, has to be smoothed and therefore contributed a positive parameter in the heat of solution. According to Miedema's theory, the heat of solution per unit surface area can be described as given in equation 5.6.

The heat of solution is originated from the contact interface between the two dissimilar atoms, which are described by the well-known Wigner–Seitz (WS) unit cells. The atomic size difference has not been considered in Miedema's theory. This difference in atomic size affects the precision of the calculation. In Miedema's theory, the contact between the two WS unit cells was ideally matched. The contact between the two dissimilar WS unit cells could not be matched ideally [Zhang *et al.* (2002)], especially for those binary transition-metal systems consisting of two metals with a considerable and large atomic size difference. In other words, the shapes of the two contacting unit cells would probably be deformed, because the contact interfaces would always differ from the surface area of the solute atom. The effect of changing contact interface area should therefore be taken into account in calculating the heat of solution as well as the standard formation enthalpy of the binary transition-metal systems.

Meanwhile, the atomic size difference would frequently lower the package density of the crystalline lattice and thus increase the binding energy between the two dissimilar atoms, because the electron cloud would become further away from the nuclei. To include these effects, a prefactor $S(c)$ is added in equation 5.15, which is defined by

$$S(C) = 1 - S_V(C) \tag{5.15}$$

Where $S_V(C)$ is named as an influential factor and c represents the alloy composition. For a binary transition-metal system, the influential factor is to describe the effect of the atom size difference on the contact interface as well as the binding energy and is expressed by a ratio between the difference of the surface area and the average area of the dissimilar atoms:

$$S_v(c) = \frac{c_B^S \left| V_A^{2/3} - V_B^{2/3} \right|}{c_A^S V_A^{2/3} + c_B^S V_B^{2/3}} \tag{5.16}$$

Equation 5.16 shows the effect of deviation of the contact interface of the two WS unit cells. The prefactor $S(c)$ is therefore expressed by

$$S(c) = 1 - \frac{c_B^S \left| V_A^{2/3} - V_B^{2/3} \right|}{c_A^S V_A^{2/3} + c_B^S V_B^{2/3}} \tag{5.17}$$

Apparently, both $S(c)$ and $S_V(C)$ depend on the alloy composition. If the two constituent metals have no atomic size difference then the prefactor $S(c)$ would be unity. $\left| V_A^{2/3} - V_B^{2/3} \right|$ is an absolute value, and therefore is always positive. Consequently, the prefactor $S(c)$ is a value within a range of $0 < S(c) < 1$. If there is atomic size difference then the heat of solution of metal A in B is expressed by the following formula

$$\Delta H_{sol}^{AinB} = \frac{S(c).V_A^{2/3}}{(n_{WS}^{=1/3})_{av}} \times \left[-P(\Delta\phi^*)^2 + Q(\Delta n_{WS}^{1/3})^2 \right] \quad (5.18)$$

Table 5.1: Atomic radius and crystal structure of the elements

Element	Atomic radius (A^o)	Crystal structure
Al	1.82	FCC
Fe	1.72	BCC

Table 5.2: Data of Al and Fe taken for thermodynamic calculation [Miedema *et al.* (1980) and Verhoven (1975)].

Element	$n^{1/3}$ (cm^{-1})	Φ (V)	K (GPa)	μ (GPa)	T_m (K)	$V^{2/3}$ (cm^2)	γ (erg/cm^2)	ΔH_f (kJ/mole)
Al	1.39	4.2	75.83	26	933	4.6	340	10.83
Fe	1.77	4.93	164.78	82	1812	3.7	756	13.86

The calculation of free energy of equilibrium phases were carried out based on the above mentioned approach. Table 5.2 gives the data of Al and Fe necessary for the calculation of Gibbs free energy. Figure 5.10 shows the variation of ΔG (for amorphous, two intermetallic compounds and crystalline solid solutions) as a function of composition for different values of d_c. It is evident that the free energy of crystalline

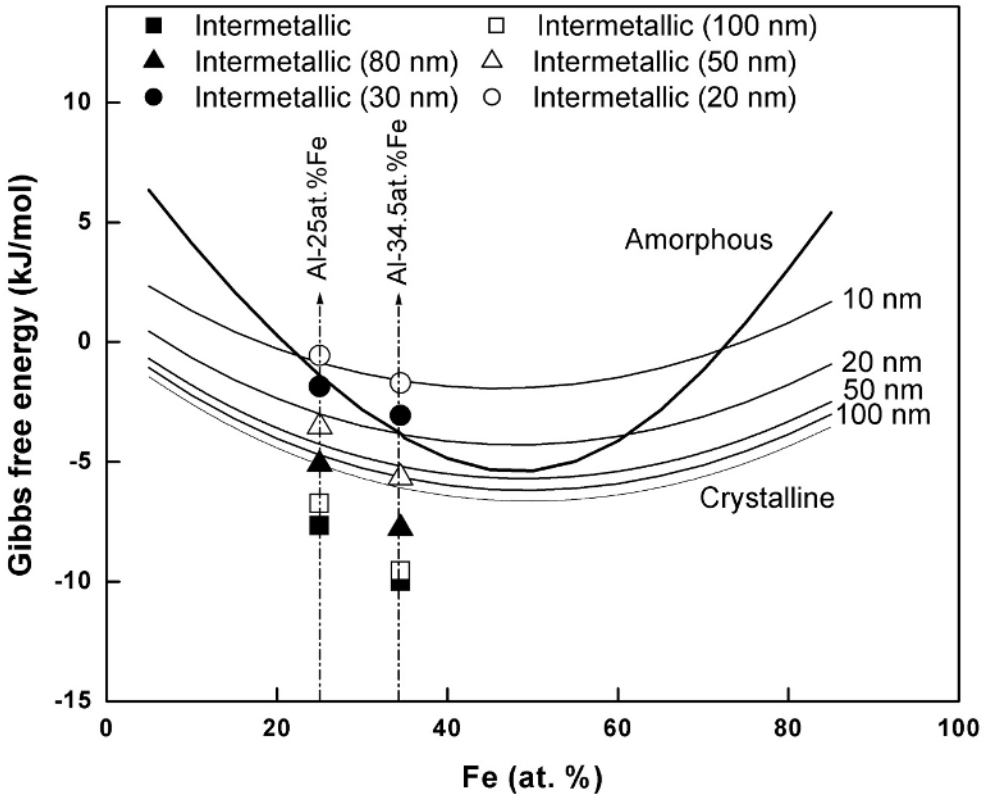

Figure 5.10: Gibbs free energy of the amorphous, solid solution and intermetallic phases of Al-Fe system as a function of composition and grain size.

solid solution of large crystallite size (where ΔG_γ can be neglected) is minimum compared to the amorphous phase. Hence it is expected to be more stable than the amorphous phase in the entire composition range. However, the intermetallics are found to be most stable phase at the corresponding composition as the Gibbs free energy is minimum. The two intermetallic phases (Al_3Fe and Al_2Fe) corresponding to the composition Al-25 at.% Fe and Al-34.5 at.% Fe are the most stable phases compared to the solid solution phase. Al_3Fe phase can transform to amorphous phase at $d_c < 20$ nm, and to convert Al_2Fe phase into amorphous state the phase grain size should be below

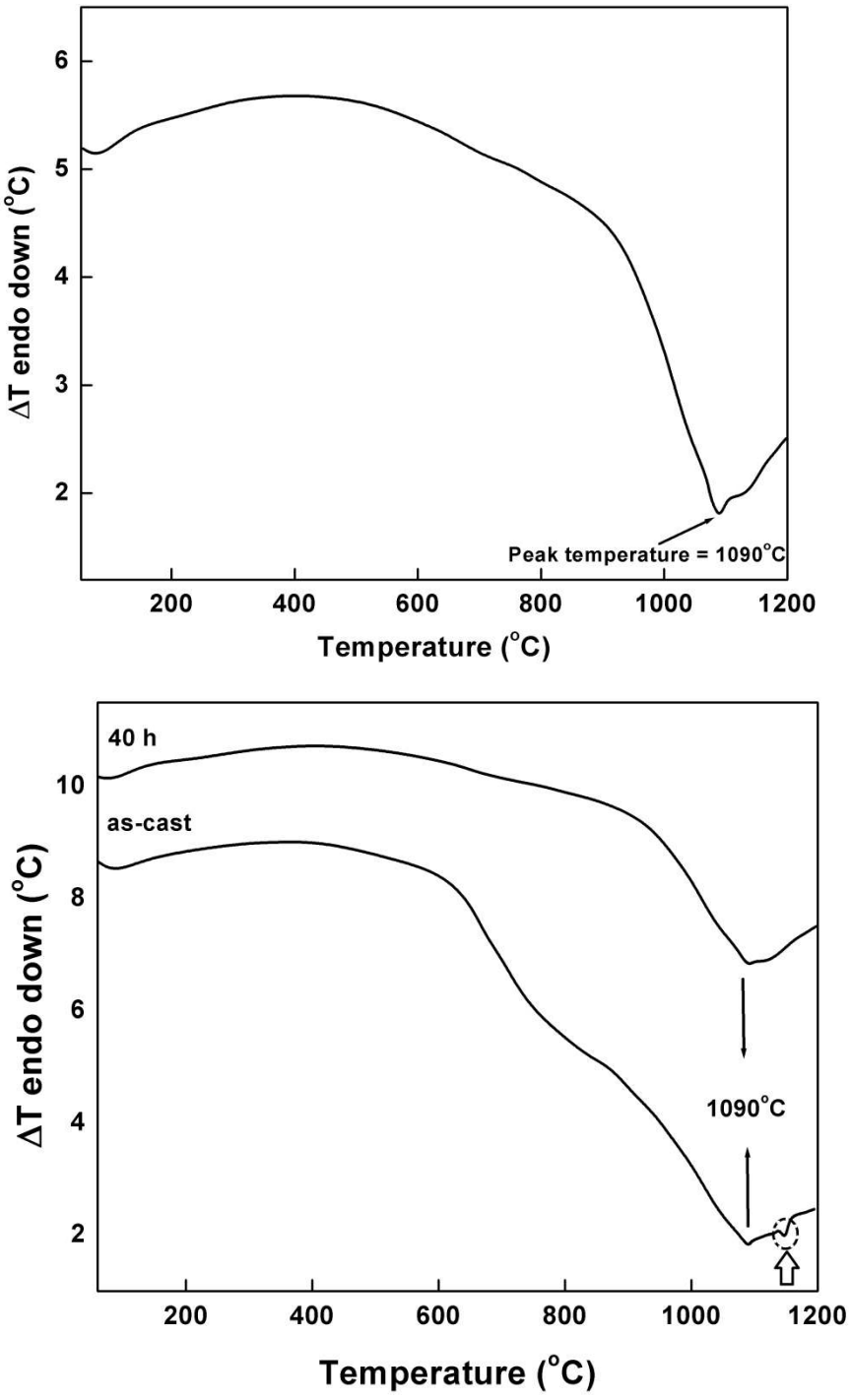

Figure 5.11: DTA traces of milled powders for (a) Al-25 at.%Fe and (b) Al-34.5 at.%Fe alloy.

30 nm. The above discussion supports the results obtained from XRD and TEM analysis of the milled powder that the phases are intermetallic prior to milling and amorphous after milling at the composition of Al-25 at.% Fe and Al-34.5 at.% Fe.

5.4 Thermal behavior of mechanically milled intermetallics

DTA trace of 50 h milled Al-25 at.%Fe intermetallic powders is shown in Fig. 5.11(a). Upon heating the as-milled powders at a constant rate of 10°C/min, Al-25 at.%Fe alloy revealed one exothermic peak at around 1090°C. Based on the equilibrium diagram of Al-Fe [Massalski (1990)], this peak corresponds to the melting point of the Al_5Fe_2 intermetallic phase, which is formed as a result of phase transformation of monoclinic Al_3Fe after high energy ball milling. DTA curves of as-cast Al-34.5 at.%Fe alloy and ball milled powder obtained after 40 h of milling are shown in Fig. 5.11(b). The thermal analyses of the as-cast alloy indicated the presence of two endothermic peaks as marked by arrows. Based on the equilibrium diagram, the first peak corresponds to the melting point (1090°C) of the Al_5Fe_2 intermetallic compound, whereas, the second peak at higher temperature of around 1149°C as marked by arrow is due to the melting of Al_2Fe. DTA trace of 40 h milled powders indicated only the presence of single exothermic peak around 1090°C corresponding to Al_5Fe_2 phase formed as result of transformation of Al_2Fe intermetallic phase to high symmetry phase Al_5Fe_2 after high energy milling. Thermal analysis results corroborate the XRD results as shown in Fig. 5.6, where the pattern corresponds to both Al_5Fe_2 and Al_2Fe phase for as-cast alloy and a single Al_5Fe_2 phase for 40 h milled powders.

5.5 Mechanical properties

Milling time dependence of Vickers hardness for Al-25 at.%Fe alloy for various milled powders is shown in Fig. 5.12(a). With increasing milling time, the hardness increased and exhibited a maximum between 20 to 30 h of milling, and then decreased. The optimum milling time for high hardness was 30 h, at which the hardness value was about 8.6 GPa. The peak in the hardness values can be attributed to the formation of intermetallic phase, η-Al_5Fe_2, and its coexistence with amorphous phase. However, microhardness of 12.4 GPa was reported for Al-20 at.%Fe alloy MA for 20 h followed by cold consolidation and subsequent annealing at 673 K for 2 h [Nayak *et al*. (2010)]. Fig. 5.12(b) shows the variation of microhardness as a function of reciprocal square root of the grain size. The hardness increases linearly with the reciprocal square root of the grain size up to a grain size of about 42 nm. Hall-Petch behaviour is thus demonstrated over the range of grain sizes from 132 nm to 42 nm, with the Hall-Petch slope describing the grain size sensitivity having a similar value to that found for conventional grain sizes. This behavior is ascribed to the grain size refinement produced by MM. However, it is interesting to note that when the crystallite sizes drops below 42 nm, the slope of the plot becomes negative. The observed effect could be an indication of softening behavior, an attribute termed as inverse H-P phenomenon [Suryanarayana (1995) and Carlton *et al*. (2007)]. Earlier researchers have proposed that hardness decreases at small grain sizes as it becomes impossible to accommodate the high density of dislocations required to form pile-up at a grain boundary [Padmanabhan *et al*. (2007) and Conrad *et al*. (2000)]. Theoretically, the critical value of the grain size can be calculated from equation 1.6.

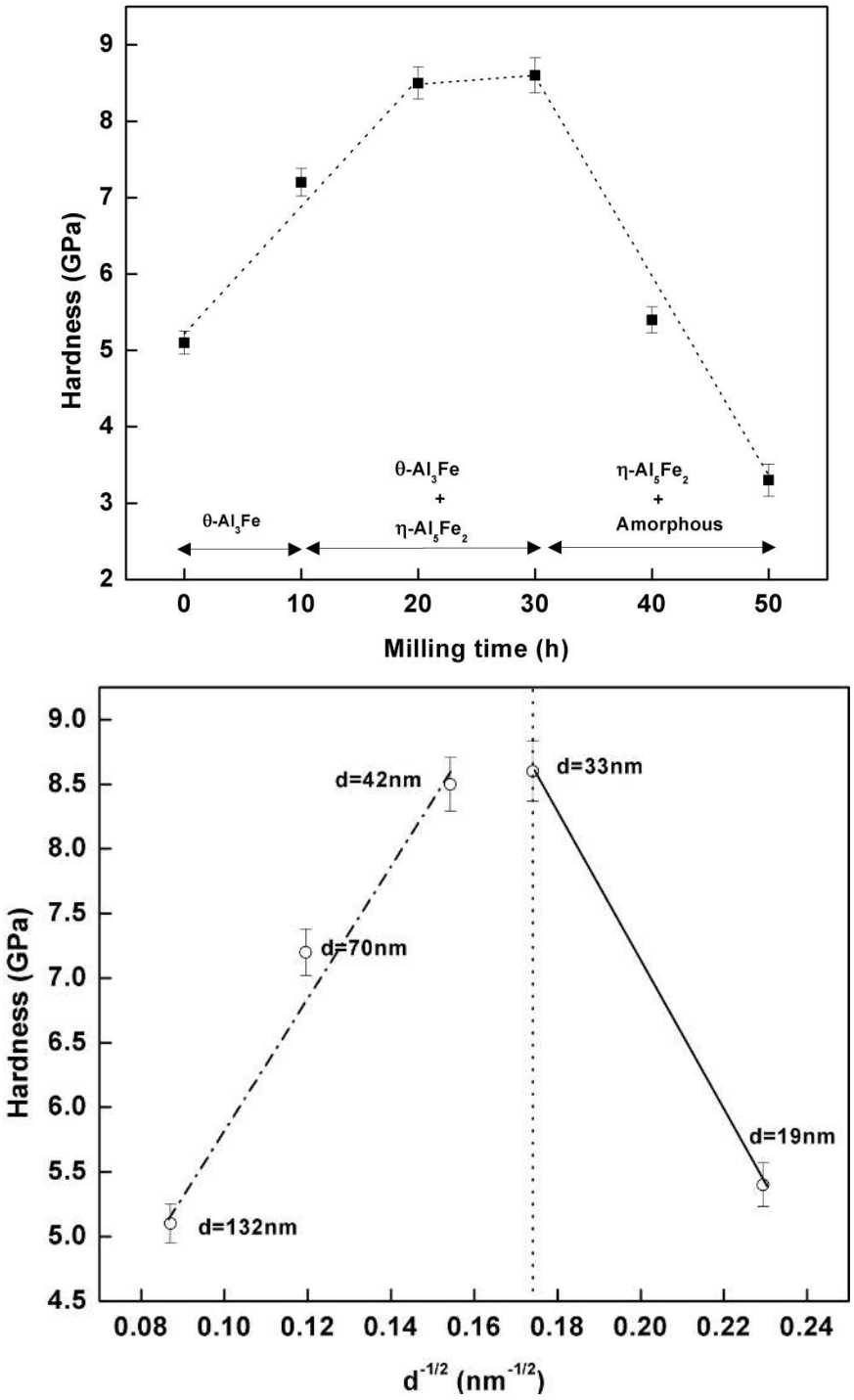

Figure 5.12: (a) Variation of microhardness as a function of milling time for Al-25 at.%Fe alloy showing the phase sequence and softening behavior, (b) Variation of microhardness as a function of square root of the grain size to test the Hall–Petch relationship for Al-25 at.%Fe alloy.

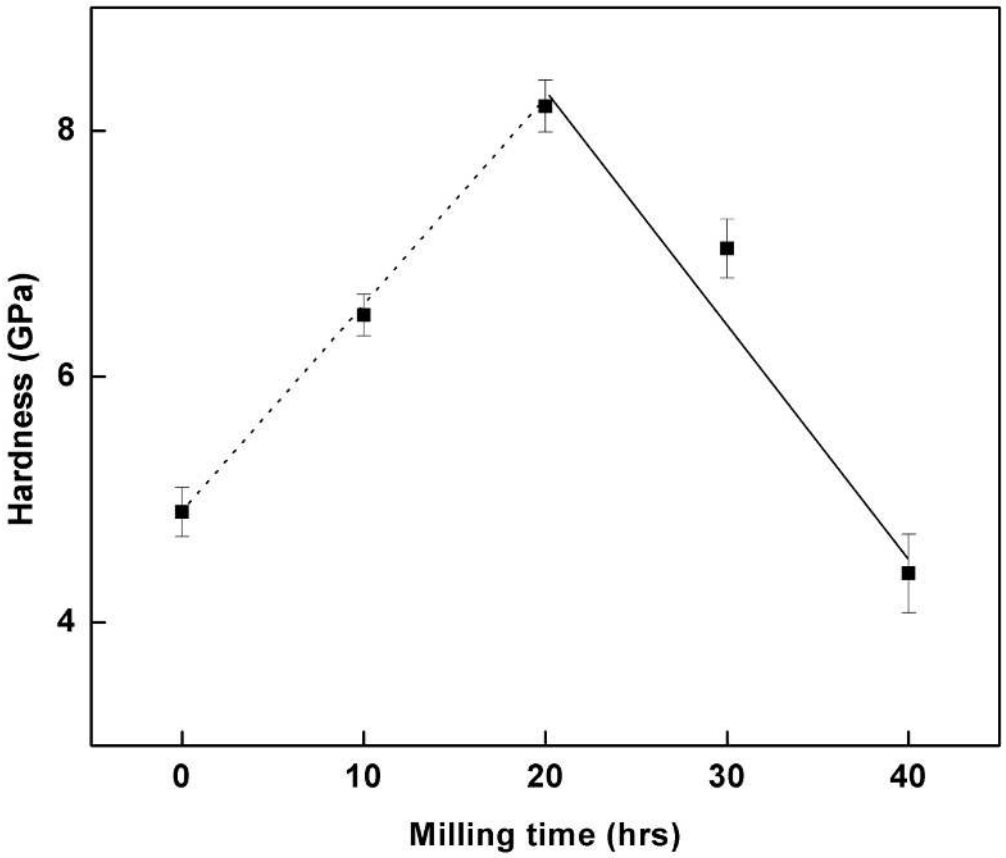

Figure 5.13: Microhardness variation as a function of milling time for Al-34.5 at.%Fe alloy showing transition from hardening to softening behavior.

To understand the discrepancy involved in dislocation pile-up mechanism related to softening behavior, the critical grain size was calculated and the value obtained was about 8 nm in comparison to experimental value of 42 nm. The difference could be due to the presence of competing/contributing effects of nanocrystalline and amorphous phase. Thus dislocation pile-up model can predict the critical grain size for nanocrystalline materials where softening occurs but fails for composite structure involving nanocrystalline and amorphous phase. Fig. 5.13 shows the variation of microhardness as a function of milling time for Al-34.5 at.%Fe alloy. It is evident from

the figure that the hardness of the alloy increased with increasing milling time at the early stage. However, it revealed softening after prolonged milling during the formation of amorphous phase. The increase in hardness values with increase in milling time is indicative of formation of amorphous phase along with crystalline intermetallic phase. Softening behavior observed at higher milling durations can be attributed to the high volume fraction of grain boundaries resulting in increased triple junction leading to grain boundary sliding [Padmanabhan *et al*. (2007)]. In case of amorphous phase, mechanisms such as decrease in interfacial excess volume and free volume model can contribute to transition from hardening to softening behavior [Li *et al*. (1997)]. There is a need to investigate this issue further in order to understand the softening behavior.

Fig. 5.14(a) and (b) present the typical load-displacement curves for intermetallic phases milled for various duration, for indentations made to peak loads of 20 mN at room temperature and shows elastic-plastic materials' response. It has been observed that there is a significant difference in the force displacement curves manifested not only by the shapes of the load-penetration depth but also the maximum penetration depth attained under the same conditions. This is due to the difference in the mechanical properties, which is greatly influenced by the microstructure [Xi *et al.* (2013) and Chromik *et al.* (2003)] of the intermetallic phases and its transformation during milling. The elastic modulus and hardness are calculated by a standard procedure according to the method of Oliver and Pharr [Oliver *et al.* (2004)]. These parameters, estimated from the curve, are given in Table 5.3. The evolution of elastic modulus with milling time indicates a relative complex effect of the phase formation/transformation in Al-Fe alloys. Severe plastic deformation induced by MM

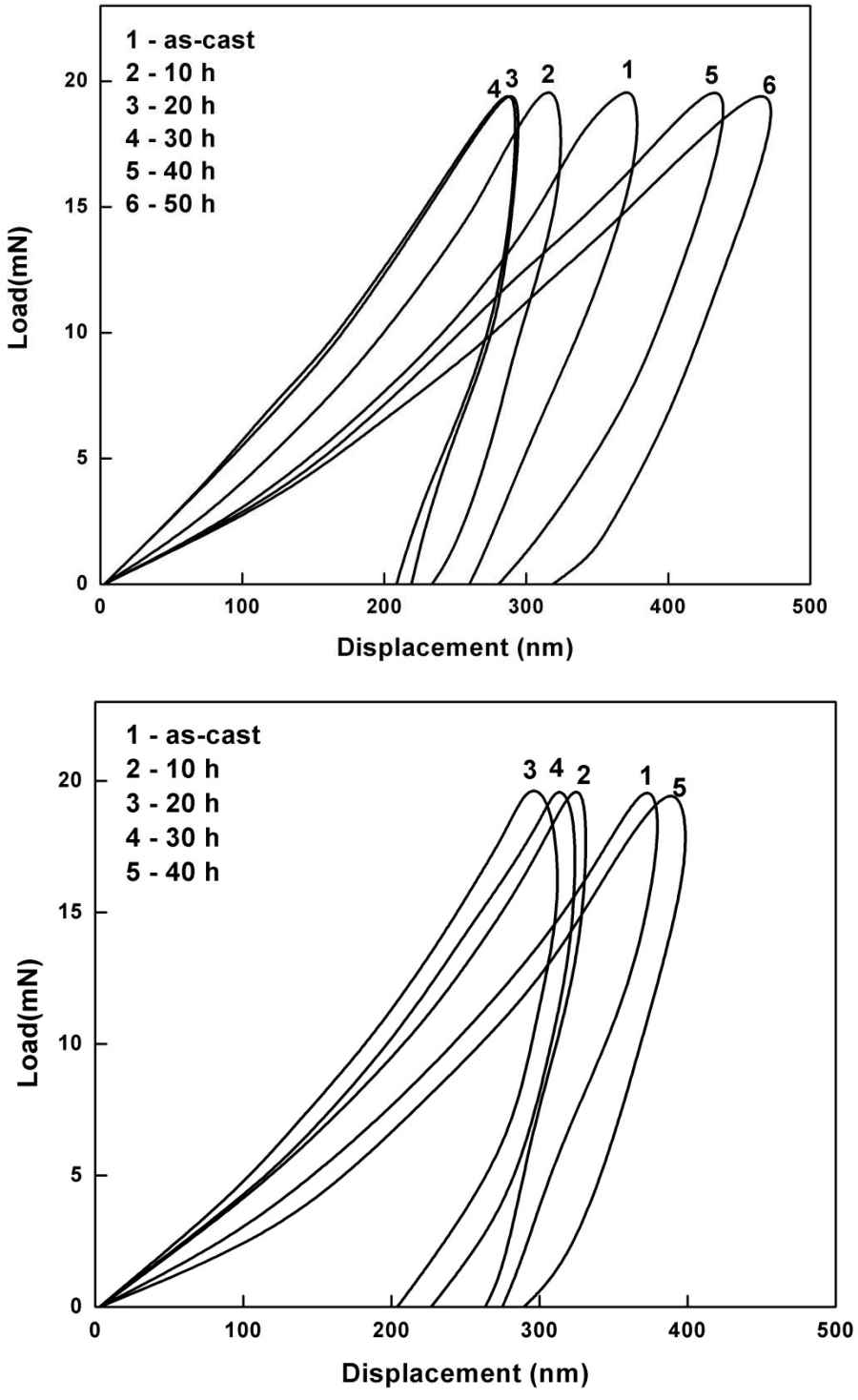

Figure 5.14:.Nanoindentation load-displacement curves for Al-25 at.%Fe and Al-34.5 at.%Fe alloy at varying milling time.

Table 5.3: Hardness and elastic modulus of alloy powders of as-cast and for various duration of milling measured by nanoindentation.

Material	**Hardness** (GPa)						**Elastic modulus** (GPa)					
	Milling time (h)											
	0	10	20	30	40	50	0	10	20	30	40	50
Al-25 at.%Fe	7.2	7.8	9.3	8.2	6.5	5.0	121	139	168	146	116	89
Al-35.4 at.%Fe	6.1	7.0	8.8	7.6	4.9	-	100	129	157	138	88	-

has great impact on elastic modulus as it represents the interatomic distance and bonding strength between atoms [Wang *et al.* (2000)]. The refinement in grain size resists grain boundary motion, resulting in increased hardness and elastic modulus at the early stages of milling. The elastic modulus has the maximum value of 168 GPa and 157 GPa at 20 h and the peak hardness values of about 9.3 GPa and 8.8 GPa for Al-25 at.%Fe and Al-34.5 at.%Fe alloys, respectively. The hardness and elastic modulus values decreased to a factor of two after longer milling time where amorphous phase formation was evidenced. Differences in average values of 0.6 GPa between microhardness and nanohardness have been observed and this effect could be ascribed to the indentation size effect (ISE) [Mukhopadhyay *et al.* (2006)].

5.6 Conclusions

1. Al-25at.%Fe and Al-34.5at.%Fe alloys resulted in Al_3Fe and Al_2Fe intermetallic phases after normal casting and annealing routes.
2. Monoclinic Al_3Fe and triclinic Al_2Fe phase was found to be unstable under high-energy milling condition and transformed to orthorhombic Al_5Fe_2 phase.
3. Structural transformation from crystalline to amorphous phase was observed in both the compositions for prolonged milling hours.

4. Mechanical property measured in microhardness testing for Al-25 at.%Fe alloy showed strengthening down to a grain size of 42 nm and Hall-Petch behavior was thus demonstrated over the range of grain sizes from 132 to 42 nm.
5. Maximum hardness was achieved for 30 h of milling where both nanocrystalline and amorphous phase co-exist.
6. At the smallest grain size (33 nm) slope of HP plot becomes negative indicating IHP behavior and dislocation pile-up model cannot intend the critical grain size at which HP relation breaks.
7. Transition from hardening to softening behavior upon milling was also observed for Al-34.5 at.%Fe alloy.
8. Contributing factors for softening observed might be due to competing effects of mechanisms such as grain boundary sliding, decrease in interfacial excess volume and free volume.